Earth and Planetary Science Letters 499 (2018) 48–61

Contents lists available at ScienceDirect

Earth and Planetary Science Letters

www.elsevier.com/locate/epsl

Downstream evolution of the thermochronologic age signal in the Brahmaputra catchment (eastern Himalaya): Implications for the detrital record of erosion

L. Gemignani [a,b,*], P.A. van der Beek [c], J. Braun [c,f], Y. Najman [d], M. Bernet [c], E. Garzanti [e], J.R. Wijbrans [a]

[a] Faculty of Earth and Life Science, Vrije Universiteit, Amsterdam, the Netherlands
[b] Dipartimento di Scienze della Terra, Universitá degli Studi di Torino, Torino, Italy
[c] Institut des Sciences de la Terre (ISTerre), Université Grenoble Alpes, CNRS, Grenoble, France
[d] Lancaster Environment Centre, Lancaster University, Lancaster, United Kingdom
[e] Dipartimento di Scienze dell' Ambiente e della Terra, Universitá degli Studi di Milano-Bicocca, Milano, Italy
[f] Helmholtz Center Potsdam, German Research Center for Geoscience (GFZ), Potsdam, Germany

ARTICLE INFO

Article history:
Received 25 April 2018
Received in revised form 11 July 2018
Accepted 14 July 2018
Available online 26 July 2018
Editor: A. Yin

Keywords:
detrital thermochronology
mixing model
present day erosion rate values
Namche Barwa syntaxis
Eastern Himalaya

ABSTRACT

The Namche Barwa massif in the eastern Himalayan syntaxis is characterized by very rapid exhumation and provides a significant proportion of the sediment flux carried by the Brahmaputra River. We present new detrital zircon fission-track (ZFT) and muscovite $^{40}Ar/^{39}Ar$ (MAr) data from modern sediments of rivers draining the eastern Himalaya. The cooling-age populations for both thermochronometers contain a characteristic <2 Ma signature related to the rapid exhumation of Namche Barwa, which can be traced hundreds of kilometers downstream from their source into the Brahmaputra foreland, despite dilution from downstream tributary catchments. To estimate present-day erosion in the catchments, we apply a mixing model based on linear inversion of the binned age distributions. The inversion predicts relative erosion rates in the syntaxial region that are an order of magnitude higher than those in upstream catchments, and about twice as high as those in the southern Himalayan catchments, consistent to first order with previous estimates of erosion-rate patterns in the eastern Himalaya. A comparison of the observed downstream evolution of age distributions with a sediment-flux model suggests that the ZFT signal can be explained by dilution from Himalayan tributaries only, whereas the MAr signal is also affected by selective sequestering (possibly through winnowing) of micas as they are transported downstream. Nevertheless, thermochronological ages <2 Ma provide a diagnostic signal of syntaxial exhumation in the sedimentary record of the eastern Himalaya; this study suggests the most robust signal to be recorded in the most proximal deposits with respect to the syntaxis.

1. Introduction

The distinctive courses of the Indus and Brahmaputra rivers draining the Himalaya, characterized by two quasi-symmetrical bends as they cut across the orogen at its western and eastern syntaxes, respectively (Fig. 1a), reflect a complex interplay of crustal deformation and drainage reorganization (Bracciali et al., 2015; Clark et al., 2004; Hallet and Molnar, 2001). The spatial link between the sharp bends and major knickpoints in these rivers within the two syntaxial massifs, which represent the loci of most rapid exhumation in the Himalaya, has sparked ongoing debates on the coupling and feedbacks between tectonics and surface processes in the syntaxes (e.g., Finnegan et al., 2008; King et al., 2016; Wang et al., 2014; Zeitler et al., 2001).

The Namche Barwa massif, occupying the eastern syntaxis, is characterized by young (<10 Ma) metamorphism, rapid and highly localized exhumation, and extreme river-incision and erosion rates (Enkelmann et al., 2011; Finnegan et al., 2008; Larsen and Montgomery, 2012; Zeitler et al., 2014). Both the timing and mechanism of rapid exhumation in the massif (King et al., 2016; Seward and Burg, 2008; Wang et al., 2014; Zeitler et al., 2014), as well as the potential links with the evolution of drainage patterns in the eastern Himalayan region (Bracciali et al., 2015; Cina et al., 2009; Lang and Huntington, 2014), remain controversial. The geochem-

* Corresponding author at: Faculty of Earth and Life Science, Vrije Universiteit, Amsterdam, the Netherlands.
E-mail address: l.gemignani@vu.nl (L. Gemignani).

https://doi.org/10.1016/j.epsl.2018.07.019

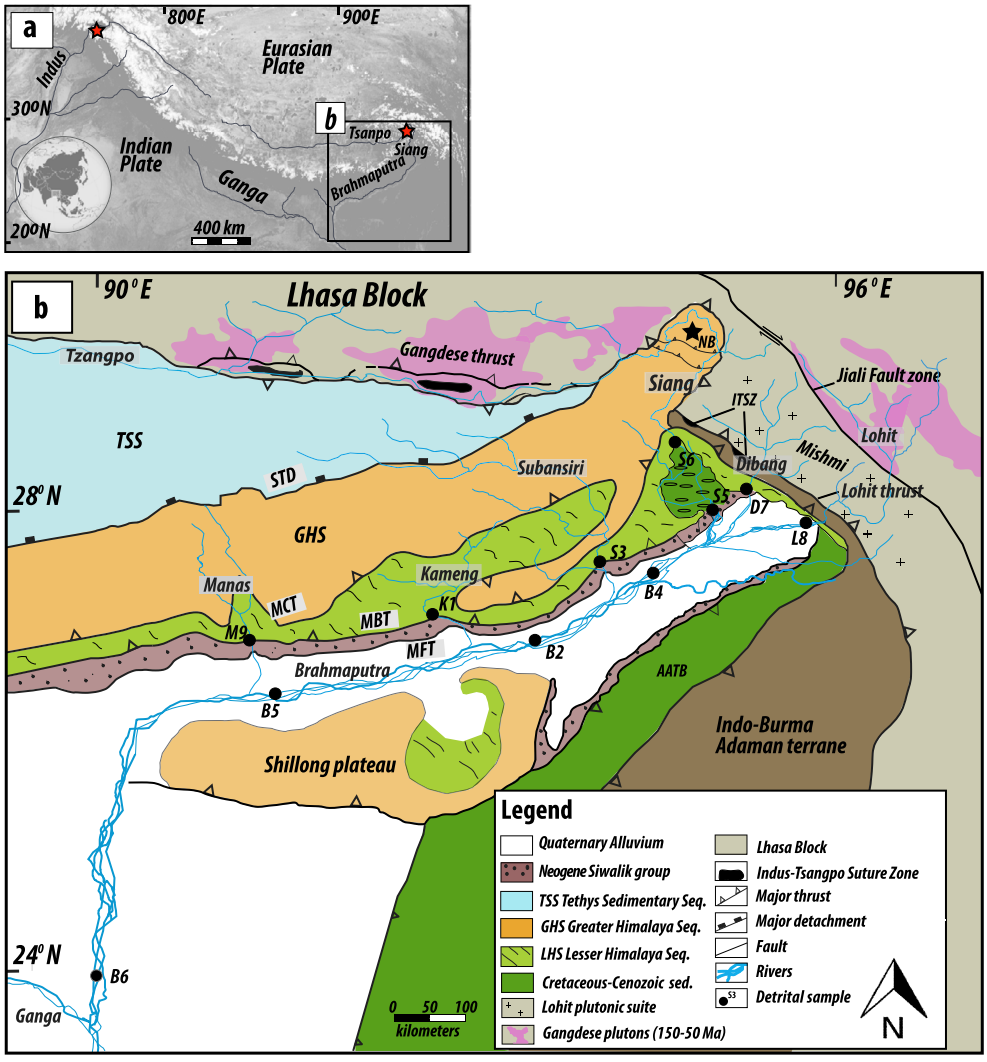

Fig. 1. Studied area in the eastern Himalaya. (a) Overview map, showing the major Himalayan rivers; western and eastern syntaxes are indicated by red stars. (b) Regional geological map (modified from Yin et al., 2010) showing the sample locations, the main tectonic features and the main rivers. Abbreviations: STD – South Tibetan Detachment; MCT – Main Central Thrust; MBT – Main Boundary Thrust; MFT – Main Frontal Thrust; ITSZ – Indus–Tsangpo Suture Zone; TSS – Tethyan Sedimentary Sequence; GHS – Greater Himalayan Sequence; AATB – Assam Akaram Thrust Belt; NB – Namche Barwa. (For interpretation of the colors in the figure(s), the reader is referred to the web version of this article.)

ical, petrographic, geochronologic and thermochronologic signatures of both the modern river sediments and the Neogene detrital record in the eastern Himalayan foreland have been used to assess: (1) the spatial pattern of present-day erosion rates in the eastern syntaxis region (Enkelmann et al., 2011; Garzanti et al., 2004; Lupker et al., 2017; Singh and France-Lanord, 2002; Stewart et al., 2008); (2) the evolution of syntaxial exhumation rates (Bracciali et al., 2016; Chirouze et al., 2013; Govin, 2017; Lang et al., 2016); and (3) the evolution of drainage patterns in the eastern Himalaya through time (Bracciali et al., 2015; Chirouze et al., 2013; Cina et al., 2009; Govin et al., 2018; Lang and Huntington, 2014; Zhang et al., 2012).

Detrital thermochronology data are central to several of the above studies because of their capacity to both record long-term (million-year scale) exhumation rates and track the distribution of present-day erosion rates (e.g., Enkelmann et al., 2011; Gemignani et al., 2017; Glotzbach et al., 2013; Ruhl and Hodges, 2005). In particular, $^{40}Ar/^{39}Ar$ thermochronology of white mica (MAr) and zircon fission-track (ZFT) analysis have been widely applied in detrital thermochronology (Bernet and Garver, 2005; Hodges et al., 2005). The nominal closure temperatures of these systems (300–450 °C and 240–360 °C respectively, depending on cooling rate, crystal size, and mineral kinetics) allow tracking of exhumation from upper- to mid-crustal depths (Reiners and Brandon, 2006). However, a detrital thermochronology signal will evolve downstream from its source as a function of numerous influences, including spatial and temporal variations in erosion rates, lateral variations of lithology and abundance of the target mineral, mechanical and chemical breakdown of the target mineral during transport, and its preferential extraction during transient storage (Bernet et al., 2004; Brewer et al., 2006; Garzanti et al., 2010; Malusà et al., 2016; Zhang et al., 2012). Robust interpretation of detrital mineral-age distributions depends on understanding these factors and their influence on the measured signal.

Here, we address this issue by systematically sampling modern river sand from the Brahmaputra catchment at increasing distances downstream from Namche Barwa, and by analyzing the downstream evolution of the detrital age signal. We utilize the unique thermochronological signal of the massif (Bracciali et al., 2016; Zeitler et al., 2014) and apply both detrital MAr and ZFT analyses to investigate potentially different behavior of these two systems. We use our data to quantitatively assess if and how the signal is transformed downstream, in order to investigate possible causes of diverging interpretations of detrital thermochronology datasets from the region (e.g., Bracciali et al., 2016; Chirouze et al., 2013; Govin, 2017; Lang et al., 2016). We also employ a recently de-

veloped stochastic mixing model (Braun et al., 2018) to predict the spatial variability of present-day erosion rates throughout the eastern Himalaya from our data supplemented with data from the literature. We compare our results to previous studies (Enkelmann et al., 2011; Garzanti et al., 2004; Lupker et al., 2017; Singh and France-Lanord, 2002; Stewart et al., 2008) in order to explore the efficacy of the detrital thermochronology signal to quantitatively constrain modern erosion rates. Finally, we estimate sediment fluxes from the different catchments sampled by our data to predict the expected degree of dilution in the detrital age signal downstream of Namche Barwa, and use this estimate to assess if additional processes modify the signal.

2. Geological setting

The 2900-km-long Yarlung–Tsangpo–Siang–Brahmaputra River flows from Tibet, via India into the Bengal Fan (Fig. 1). The Yarlung–Tsangpo is sourced near Mount Kailash in southwestern Tibet and flows >1000 km eastwards, along strike of the Himalaya, along the India–Asia suture zone. The river bends sharply at the eastern Himalayan syntaxis and continues to the south through the Tsangpo gorge, forming a >2-km-high knickpoint as it crosses the Namche Barwa massif (e.g., Finnegan et al., 2008; Wang et al., 2014; Zeitler et al., 2001).

2.1. The Lhasa block and the Himalayan units

The Yarlung–Tsangpo suture zone (YTSZ) defines the collisional contact between the Indian and Asian continental blocks (Gansser, 1980). North of the YTSZ, the Lhasa block is composed of Paleozoic and Mesozoic meta-sedimentary sequences intruded by Cretaceous–Paleogene calc-alkaline plutonic rocks of the Gangdese (Transhimalayan) batholith (Yin and Harrison, 2000). South of the suture zone, the Himalaya is subdivided from north to south into four main tectonic units (e.g., Hodges, 2000; Fig. 1b): the Tethyan Sedimentary Sequence (TSS), Greater Himalayan Sequence (GHS), Lesser Himalayan Sequence (LHS), and Sub-Himalaya (including the Siwalik Group). The TSS comprises Paleozoic–Eocene rocks deposited on the Indian plate margin and is separated from the underlying GHS by the extensional South Tibetan Detachment system (STDS). The GHS is composed of metamorphic rocks intruded by Miocene leucogranite bodies. An inverse regional shear zone, the Main Central Thrust (MCT), separates the GHS and LHS. Exhumation and metamorphism of the GHS is dated at ~25–17 Ma (Hodges, 2000). The LHS consists of meta-sedimentary rocks of Precambrian to Mesozoic age, that are deformed in a complex fold-and-thrust belt (e.g., DeCelles et al., 2016). Finally, the Siwalik Group consists of Neogene foreland-basin deposits separated from the LHS by the Main Boundary Thrust (MBT).

2.2. Eastern syntaxis; Namche Barwa massif

In the easternmost Himalaya, the suture zone changes strike >90° around the Namche Barwa massif (Fig. 1b), a northeast-verging crustal-scale antiform characterized by young (<10 Ma) metamorphism and rapid (at least ~3–5 km/Myr and possibly up to 10 km/Myr; Bracciali et al., 2016; Zeitler et al., 2014) exhumation. Estimates for the onset of rapid exhumation vary from around 10 Ma (Zeitler et al., 2014) to 3–4 Ma (Seward and Burg, 2008) or less (Bracciali et al., 2016; Wang et al., 2014). Proposed mechanisms to explain the rapid exhumation and erosion rates at Namche Barwa include: (1) crustal-scale buckling (Burg et al., 1997), possibly associated with northward migration of the syntaxis (King et al., 2016; Seward and Burg, 2008); (2) localized uplift above the curved underthrusting Indian plate at the indenter corner (Bendick and Ehlers, 2014); (3) vigorous erosional downcutting following capture of the Yarlung–Tsangpo by the Siang–Brahmaputra River, weakening the crust and resulting in a "tectonic aneurysm" (Zeitler et al., 2001, 2014).

The Namche Barwa massif comprises Indian plate rocks and is bounded to the west, north and east by the Lhasa block and the Transhimalayan plutonic belt (Fig. 1b). Southeast of the syntaxis, the Lohit plutonic complex is separated from underlying mélange, gneiss and schist units by northwest–southeast aligned thrusts orthogonal to the Himalayan strike (Haproff et al., 2018; Misra, 2009); the Lohit plutonic complex and underlying mélange can be correlated to the Gangdese batholith and Yarlung–Tsangpo suture zone, respectively (Yin and Harrison, 2000). The Siang window to the south of Namche Barwa (Fig. 1b) exposes Meso-Cenozoic sedimentary and mafic volcanic rocks (Acharyya, 2007).

2.3. Bedrock thermochronology data from the eastern Himalaya

In order to provide the context for our detrital thermochronology data, we present a summary of available bedrock thermochronology data from the eastern Himalaya (Fig. 2). Within the Lhasa terrane and Gangdese batholith, mica and feldspar $^{40}Ar/^{39}Ar$ ages suggest cooling from mid-crustal temperatures between ~20 and 30 Ma (Copeland et al., 1995; Yin et al., 1999). Apatite fission-track (AFT) and (U–Th)/He (AHe) ages suggest rapid cooling to surface temperatures during the middle Miocene (~15–20 Ma; Li et al., 2016). Likewise, AFT, AHe and zircon (U–Th)/He (ZHe) thermochronology data from the northern TSS indicate rapid middle-Miocene cooling (Li et al., 2015), whereas MAr, ZHe and AFT ages from the footwall of the STDS are ~11–16 Ma, implying rapid (tectonic) exhumation at this time (Carrapa et al., 2016; Kellett et al., 2013; Schultz et al., 2017).

In the eastern syntaxis, *in-situ* thermochronology data show a bulls-eye pattern around the Namche Barwa massif (Bracciali et al., 2016; Zeitler et al., 2014; Fig. 2). Both medium- (biotite $^{40}Ar/^{39}Ar$) and low-temperature (ZHe, AFT) systems show ages <2 Ma, which extend toward the NE in the Parlung River basin (Fig. 2; Seward and Burg, 2008; Zeitler et al., 2014). ZHe ages of 4–14 Ma and AFT ages <2.5 Ma have been reported from the Siang window (Salvi et al., 2017).

Further west in Arunachal Pradesh, AFT and ZFT ages from the GHS are ~1–3 Ma and ~5–9 Ma, respectively, whereas they are ~6–13 and ~11–14 Ma in the LHS (Adlakha et al., 2013). MAr cooling ages reported from the GHS of Arunachal Pradesh are ~8–12 Ma (Yin et al., 2010). In Bhutan, AHe, AFT and ZHe ages are somewhat older and show consistent patterns, with a northward increase of cooling ages across the LHS followed by a decrease north of the MCT and a renewed increase toward the STD (Adams et al., 2015; Coutand et al., 2014; Long et al., 2012). ZFT ages are ~8–17.5 Ma, whereas AFT and AHe ages are ~2.5–7 Ma. MAr ages across the MCT in eastern Bhutan are ~9–14 Ma and ~1 Ga in the LHS (Long et al., 2012; Stüwe and Foster, 2001).

The youngest AHe, AFT and ZHe ages from the Shillong plateau are ~8–14 Ma, with older ages of up to ~100 Ma for AHe/AFT and ~400 Ma for ZHe (Biswas et al., 2007; Clark and Bilham, 2008). No thermochronology data are available for the Lohit and Dibang drainage basins. In summary, ZFT and MAr ages <2 Ma have only been encountered in rocks from the Namche Barwa massif.

3. Methods

3.1. Detrital thermochronology

We sampled bulk modern sediments from the Brahmaputra River at regular intervals downstream of the syntaxis, from its entry point into the Assam plain at Pasighat to its confluence with the Ganga, nearly 1000 km downstream of the Namche Barwa. We

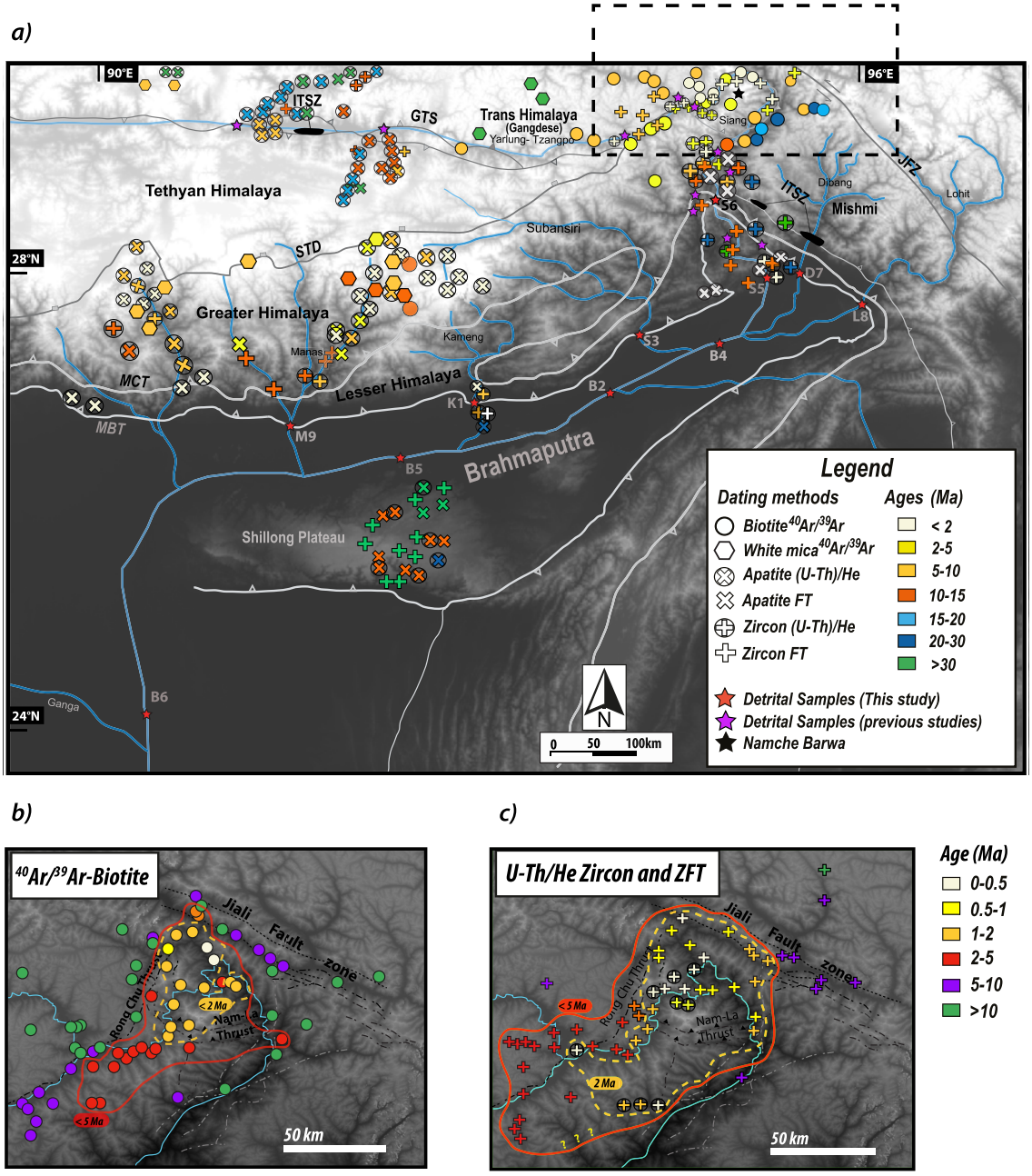

Fig. 2. (a) Digital elevation model (DEM) of the eastern Himalaya showing major tectonic features, main rivers, and published bedrock thermochronological ages; ages are represented by a color code and thermochronological techniques by different symbols (see legend in (a)). In areas with high sample density, symbols represent averages of several data points. Data were compiled from the following sources: Adams et al. (2015); Adlakha et al. (2013); Biswas et al. (2007); Clark and Bilham (2008); Copeland et al. (1995); Coutand et al. (2014); Finnegan et al. (2008); Grujic et al. (2006); Li et al. (2015, 2016); Salvi et al. (2017); Stüwe and Foster (2001); Yin et al. (1999, 2010); Zeitler et al. (2014). Dashed line shows location of insets (b) and (c): zoom on the eastern syntaxis showing in-situ biotite $^{40}Ar/^{39}Ar$ ages (b) and zircon (U–Th/He) and fission-track ages (c), modified from Zeitler et al. (2014). Note that the color code (to the right of c) is common to these two panels but different from that in (a). The 2-Ma and 5-Ma age contours are shown with a dotted yellow line and continuous red line, respectively.

also sampled the main tributaries to the Brahmaputra River; the Siang, Dibang, Lohit, Subansiri, Kameng and Manas Rivers (Table 1; Figs. 1 and 2). We sampled in October, after the main monsoon season, and targeted dry sand banks within the main channel of the rivers away from major tributaries, collecting sand from different locations on each bank to augment the representativeness of the samples. Both detrital MAr and ZFT analysis was applied on all samples where possible. Detailed analytical techniques are reported in Appendix A. Resulting age distributions were decomposed into age peaks (Table 2) using the mixture-model function of the DensityPlotter program (Vermeesch, 2012) for MAr data and Binomfit peak fitting (Stewart and Brandon, 2004) for ZFT ages.

3.2. Inversion of age distributions

We used a linear inversion method to predict the spatial variability in erosion rates between the different sampled catchments from the binned age distributions, and compared the outcome to previous studies of erosion rates in the eastern Himalaya in order to quantitatively assess the robustness and representativeness of the detrital age patterns. Unlike other methods that used detrital age distributions together with present-day hypsometry to assess the spatial variation of erosion (e.g., Brewer et al., 2006; Ruhl and Hodges, 2005; Stock et al., 2006), our approach requires no *a-priori* information on the spatial distribution of ages in the

Table 1
Summary of the new and published data used for mapping the spatial variation of erosion rates in the Eastern Himalaya.

River	Sample short label	Sample full label	Lat. (N)	Long. (E)	Method	References
Main river trunk						
Yarlung–Tsangpo	T1	TG05-40a	29°21.281′	90°43.589′	MAr + ZFT	Bracciali et al. (2016)
Yarlung–Tsangpo	T2	TG05-41a	29°15.529′	91°39.909′	MAr + ZFT	Bracciali et al. (2016)
Yarlung–Tsangpo	302	302	29°25.989′	94°31.591′	ZFT	Stewart et al. (2008)
Yarlung–Tsangpo	P	P	29°36.442′	94°56.189′	ZFT	Enkelmann et al. (2011)
Siang	A	A-Kapu			MAr + ZFT	Lang et al. (2016)
Siang	**S6**	**Lg-06**	**28°38.208′**	**95°01.503′**	**MAr**	**This study**
Siang	B	B-Nubo	28°34.599′	95°04.212′	MAr	Lang et al. (2016)
Siang	C	C-Pasighat	28°05.920′	95°17.630′	MAr	Lang et al. (2016)
Siang	S	S-Pasighat	28°05.982′	95°17.631′	ZFT	Enkelmann et al. (2011)
Siang	**S5**	**Lg-05-Pasighat**	**28°06.140′**	**95°17.984′**	**MAr + ZFT**	**This study**
Siang	Q	–	29°02.963′	94°54.610′	ZFT	Enkelmann et al. (2011)
Siang	R	–	28°34.628′	95°04.222′	ZFT	Enkelmann et al. (2011)
Brahmaputra	**B4**	**Lg-04**	**27°26.664′**	**94°45.531′**	**MAr + ZFT**	**This study**
Brahmaputra	**B2**	**Lg-02**	**26°47.308′**	**93°30.356′**	**MAr + ZFT**	**This study**
Brahmaputra	**B5**	**Lg-10**	**26°11.965′**	**91°46.349′**	**MAr + ZFT**	**This study**
Brahmaputra	**B6**	**Lg-11**	**23°53.351′**	**89° 41.106′**	**MAr + ZFT**	**This study**
Tributaries to the main trunk upstream of the Namche Barwa syntaxis						
–	H	H	29°36.385′	94°56.212′	ZFT	Enkelmann et al. (2011)
Himalayan tributaries						
Yang Sang	Y	–	28°58.123′	94°54.583′	MAr	Lang et al. (2016)
Siyom	X	–	28°13.160′	94°51.953′	MAr	Lang et al. (2016)
Yanme	Z	–	28°11.067′	95°13.411′	MAr	Lang et al. (2016)
Subansiri	**S3**	**Lg-03**	**26°47.308′**	**93°30.356′**	**MAr + ZFT**	**This study**
Kameng	**K1**	**Lg-01/KAM30***	**26°11.931′**	**91°46.297′**	**MAr + ZFT**	**This study**
Manas	**M9**	**Lg-09**	**26°46.955′**	**90°57.441′**	**MAr**	**This study**
–	I	–	28°57.700′	94°51.826′	ZFT	Enkelmann et al. (2011)
–	J	–	28°54.599′	94°46.441′	ZFT	Enkelmann et al. (2011)
Yang Sang	K	–	28°58.700′	94°54.283′	ZFT	Enkelmann et al. (2011)
–	L	–	28°20.184′	94°57.460′	ZFT	Enkelmann et al. (2011)
–	M	–	28°13.187′	94°51.321′	ZFT	Enkelmann et al. (2011)
Yanme	N	–	28°11.099′	95°13.211′	ZFT	Enkelmann et al. (2011)
Lohit / Mishmi hills tributaries						
Dibang	**D7**	**Lg-07**	**28°09.496′**	**95°40.743′**	**MAr + ZFT**	**This study**
Lohit	**L8**	**Lg-08**	**27°26.664′**	**94°45.531′**	**MAr**	**This study**

Abbreviations: MAr: muscovite $^{40}Ar/^{39}Ar$; ZFT: zircon fission-track.

Table 2
Summary of the new detrital MAr and ZFT data, and peak-fitting results.

Sample	Analysis	*N*	Age range	$N < 2$ Ma	$N < 5$ Ma	P1	P2	P3	P4	P5
S6	MAr	69	0.5–45	5	16	6.3 ± 0.2 [34]	11.6 ± 0.2 [15]	19.9 ± 0.2 [40]	28.3 ± 0.6 [9]	45.7 ± 1.8 [2]
S5	MAr	97	0.5–60	4	4	0.6 ± 0.1 [4]	16.3 ± 0.5 [28]	23.4 ± 0.1 [60]	32.0 ± 0.2 [6]	43.7 ± 0.4 [3]
D7	MAr	41	16–54	0	0	24.2 ± 0.1 [11]	31.0 ± 0.1 [22]	38.0 ± 0.0 [17]	41.6 ± 0.1 [19]	47.2 ± 0.1 [31]
L8	MAr	43	4.1–71	0	1	7.1 ± 0.3 [6]	21.0 ± 0.0 [26]	23.4 ± 0.1 [30]	28.7 ± 0.1 [26]	48.0 ± 0.1 [12]
B4	MAr	80	0.5–430	2	9	1.1 ± 0.1 [13]	10.6 ± 0.1 [48]	18.6 ± 0.1 [20]	22.4 ± 0.1 [19]	38.0 ± 0.4 [3]
S3	MAr	64	2.6–28	0	4	3.8 ± 0.1 [7]	9.2 ± 0.1 [13]	10.6 ± 0.0 [43]	16.2 ± 0.2 [25]	24.0 ± 0.1 [12]
B2	MAr	68	1.3–423	4	6	1.6 ± 0.0 [7]	7.4 ± 0.1 [18]	11.9 ± 0.1 [27]	19.0 ± 0.1 [38]	27.0 ± 0.0 [10]
K1	MAr	66	0.6–118	2	8	2.4 ± 0.3 [10]	6.4 ± 0.0 [21]	9.2 ± 0.2 [27]	13.9 ± 0.1 [36]	27.0 ± 0.2 [5]
B5	MAr	82	0.3–526	6	9	1.7 ± 0.0 [11]	11.5 ± 0.0 [30]	17.0 ± 0.0 [26]	24.0 ± 0.0 [26]	42.0 ± 0.2 [7]
M9	MAr	43	6.1–42	0	0	6.0 ± 0.7 [5]	9.5 ± 0.0 [28]	11.9 ± 0.0 [44]	15.6 ± 0.1 [20]	21.5 ± 0.2 [3]
B6	MAr	152	1.6–259	1	4	11.0 ± 0.0 [40]	16.3 ± 0.0 [36]	27.0 ± 0.0 [17]	29.3 ± 0.0 [4]	46.2 ± 0.1 [3]
S5	ZFT	103	0.5–66.4	12	46	1.0 ± 0.2 [11]	3.1 ± 0.6 [35]	7.9 ± 1.3 [28]	18.6 ± 3.3 [25]	
D7	ZFT	96	3.5–115.4	0	0	8.8 ± 2.2 [15]	14.1 ± 2.3 [47]	25.6 ± 4.8 [35]	56.6 ± 36.3 [4]	
B4	ZFT	100	0.5–46.4	16	42	1.5 ± 0.4 [27]	4.7 ± 0.8 [28]	12.5 ± 2.5 [15]	23.9 ± 3.8 [31]	
S3	ZFT	64	2.4–43.5	0	8	5.0 ± 0.9 [22]	10.4 ± 1.5 [52]	16.8 ± 3.2 [20]	29.4 ± 9.0 [6]	
B2	ZFT	74	0.8–92	5	15	1.2 ± 0.4 [7]	4.4 ± 1.8 [14]	8.9 ± 1.4 [53]	16.9 ± 2.9 [27]	
K1	ZFT	94	2.6–272.6	0	14	6.4 ± 0.6 [51]	17.4 ± 1.9 [38]	138.9 ± 25.2 [11]		
B5	ZFT	100	0.2–93.6	20	33	1.2 ± 0.2 [30]	8.8 ± 1.4 [44]	22.1 ± 3.8 [26]		
B6	ZFT	78	0.6–76.1	9	39	2.7 ± 0.4 [39]	9.3 ± 1.4 [47]	34.9 ± 6.1 [14]		

Note: *N* is the number of single-grain analyses: P is the peak age in Ma ± 1σ of the computed age population. For MAr analysis the deconvolved age populations were calculated with the Mixture Model function of the DensityPlotter program (Vermeesch, 2012) and for the ZFT ages Binomfit peak fitting (Stewart and Brandon, 2004) was used; in brackets is the size of the age population in %.

source catchments but relies on the downstream evolution of detrital age patterns alone. In principle, if these age patterns change strongly between two successive sampling sites, the intervening catchment area has to be eroding relatively quickly (accounting for the size of the catchment and the relative concentration of the target mineral) and to supply a distinct age population to the river sediments. In contrast, if the age distribution does not change significantly between successive sites, then the intervening catchment area either has an age pattern that is indistinguishable from that of the upstream river sediments, or does not provide a large flux of target minerals to the river (because it is small, eroding slowly, and/or does not contain a high concentration of the target

mineral). The model can also be applied to tributary catchments, but in this case it will only return a precise estimate if the tributary erosion rate is smaller than that of the trunk catchment; if the tributary erosion rate is larger than only a minimum estimate that is equal to the trunk erosion rate is obtained. The method is based on solving a coupled system of linear equations to invert for both relative erosion rate and age pattern in the different source catchments. It is fully described in Braun et al. (2018); a concise description of the model and its main equations is provided in Appendix D.

For the modeling, we completed our new dataset with additional data from the literature (Bracciali et al., 2016; Enkelmann et al., 2011; Lang et al., 2016; Stewart et al., 2008; Table 1; Figs. 4, 5). The linear inversion was run separately for the MAr and the ZFT data, using bin ages of <5 Ma, 5–10 Ma, 10–20 Ma, 20–50 Ma, and >50 Ma. The bins were chosen so as to include the most commonly occurring age peaks in all samples (Table 2). Numerous model runs were performed to test the sensitivity of the inversion to the number and the widths of the chosen bins. We found that, for realistic bin ages and widths, the mixing model predicts spatial patterns of erosion rates that do not vary strongly (Supplementary Table B3). We assess the uncertainty of our estimates of relative erosion rate by a bootstrapping approach, in which we apply the inversion to a large number of random sub-samples (with replacement) of the observed age distribution.

3.3. Concentration factors

The mixing model requires information on the relative concentration of the target minerals in the different sampled catchments (cf. Appendix B; Eqs. (B8), (B9)). Variable mineral concentrations can be a source of bias when interpreting detrital age distributions, and are observed even in units with similar lithology (Malusà et al., 2016). We have estimated the abundance of zircon and muscovite in source catchments based on their concentrations in river sands (Table 3). Grain sizes of 100–500 μm, similar to those of the dated minerals, were used. Mineral concentrations were obtained from quantitative assessment of petrographic and heavy-mineral modes by point-counting of thin sections and grain mounts under the microscope, combined with weighing the dense sediment fraction separated with heavy liquids (>2.90 g cm^{-3}).

4. Results

Detrital thermochronology data are synthesized in Table 2 and Fig. 3; detailed analytical results are provided in Supplementary Tables A1 and A2. ZFT data for the Kameng River sample (K1) were previously reported by Chirouze et al. (2013).

4.1. Detrital muscovite $^{40}Ar/^{39}Ar$ (MAr) ages

The Brahmaputra samples (B2, B4, B5, B6) all yield broad ranges of ages, with peaks from ~2 Ma to ~40 Ma. 9–12% of the ages are <5 Ma and ~5% are <2 Ma, except in the most downstream sample B6, which has <1% ages <2 Ma. Sample B4 has 10% pre-Himalayan ages (>50 Ma), other samples have <5% of those ages. 7% of the cooling ages are <2 Ma in the Siang sample (S6); however the major age peaks are at ~6 Ma, ~11 Ma and ~20 Ma. The next sample downstream (S5) has a similar percentage of ages <2 Ma, with no grains ~2–10 Ma; the large majority of grains is in the range ~15–30 Ma. Eastern tributaries (Dibang, D7; Lohit, L8) show a large majority of ages >20 Ma; D7 contains no ages <20 Ma, while L8 has a small age peak <10 Ma. Samples from rivers draining the southern Himalayan flank (Subansiri, S3; Kameng, K1; Manas, M9) show major age peaks between ~10–15 Ma, with smaller peaks around 3 Ma (S3, K1) and 6 Ma (K1, M9).

4.2. Detrital zircon fission-track (ZFT) ages

Brahmaputra samples all have a majority of ages <10 Ma, with significant age peaks around 2 Ma (except for B2, where this peak is minor) and 9–12 Ma. 8–23% of the ages are >20 Ma. The Siang sample (S5) yields a positively skewed distribution with a majority of <5 Ma ages (55%; 13% of ages <2 Ma). The Dibang sample (D7) shows a broad age peak at 15–25 Ma (~80%); 17% of the ages are >30 Ma. The Himalayan tributaries (S3, K1) have large age peaks at 5–10 Ma, encompassing ~50% of the data, and an older peak at ~17 Ma.

4.3. Inversion of detrital age distributions

The inversion results, i.e., the distributions of predicted relative erosion-rate values using the MAr and ZFT age distributions, are presented in Figs. 4 and 5, respectively. Note that the inversion predicts the relative (non-dimensional) erosion-rate values of each catchment, with respect to the most upstream catchment (in our case represented by sample T1 on the Yarlung–Tsangpo upstream of Namche Barwa). We rescaled these values so that the average for all catchments, weighted by catchment size and target-mineral concentration, is equal to 1. We report the median relative erosion-rate values, with the standard deviations around the mean as the credible intervals, in Supplementary Tables B1 and B2. The fit of the predicted and observed age distributions for each sample are shown in Supplementary Figs. S1 and S2.

The inversion of the MAr dataset predicts low relative erosion-rate values upstream of the syntaxis (median values of ~2×10^{-3} for samples T1 and T2). Downstream of Namche Barwa, relative erosion-rate values increase five- to two-hundred-fold in samples S6 (median value ~0.01) through S5* (a composite sample for the Pasighat site constructed by combining our sample S5 and sample C from Lang et al., 2016; median value ~0.4), as significant proportions of young (<10 Ma) ages are mixed into the populations. Lower relative erosion-rate values (~0.01) are predicted for the Lohit and Dibang tributaries, as their characteristic age distributions, with large proportions of old ages, do not significantly influence the trunk-stream distribution. The model predicts relatively high relative erosion-rate values with medians of ~0.05–0.15 for the Brahmaputra catchments and their south-flank Himalayan tributaries. The highest relative erosion-rate values (~1) are predicted for the most downstream catchment (B6) and its tributary the Manas (M9).

Inversion of the ZFT data similarly leads to low predicted relative erosion-rate values along the Yarlung–Tsangpo upstream of the syntaxis: samples T1, T2, 302 and P all have median values of <0.05 (and for two of them, <0.01). The estimated relative erosion-rate values increase by an order of magnitude (median values ~0.15) as the river crosses the Namche Barwa massif (samples H and Q), and then by another order of magnitude (median values >1) for the tributary samples I–K draining the massif and the trunk-stream sample R just downstream. All of these samples are characterized by a large bin of <5 Ma ages. Downstream of the massif, relative erosion-rate values drop again by an order of magnitude (median values ~0.1) both in the tributary samples L–N and the trunk-stream sample at Pasighat (combination of S5, sample 301 from Stewart et al., 2008, and sample S from Enkelmann et al., 2011). The Dibang sample (D7) shows different behavior for ZFT than for MAr: relative erosion-rate values are predicted to be relatively high (median value ~0.1) because it contributes to the large proportion of >10 Ma ages observed in the downstream trunk sample B4. The foreland Brahmaputra samples and their southern Himalayan tributaries show contrasting behavior: samples B4 and B5, as well as the Kameng River, suggest median relative erosion-rate values of ~0.2, consistent with the MAr

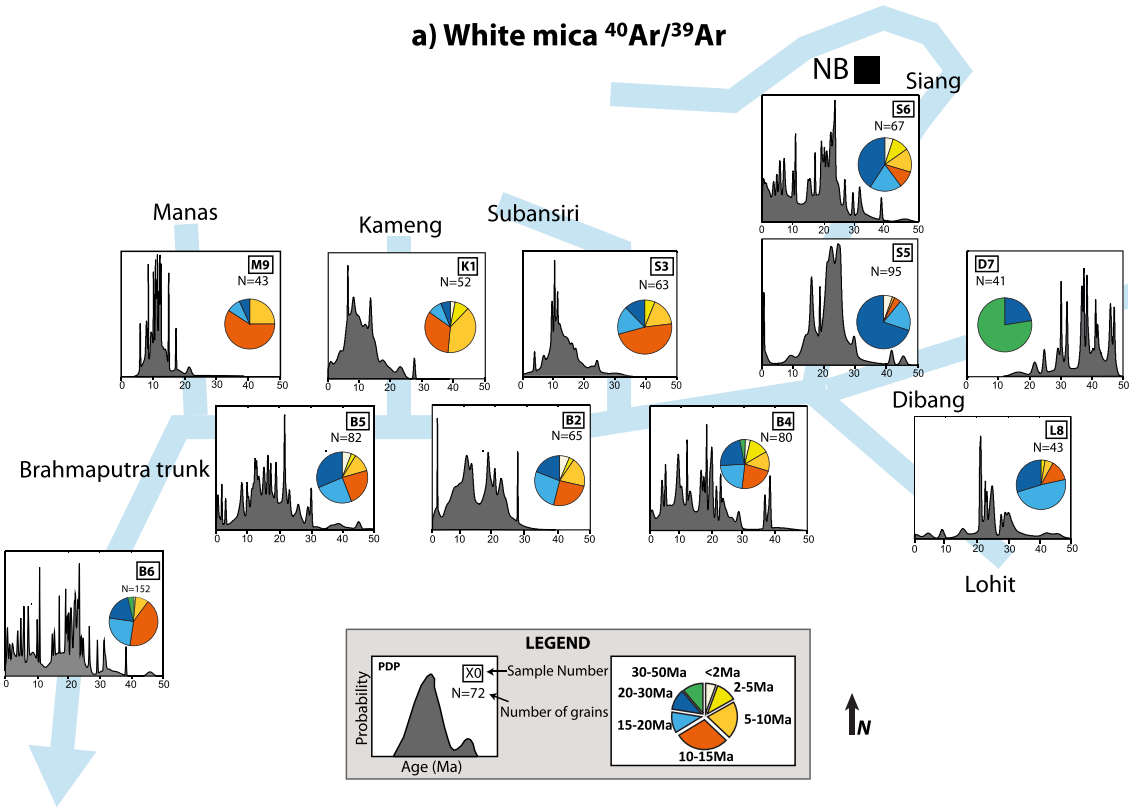

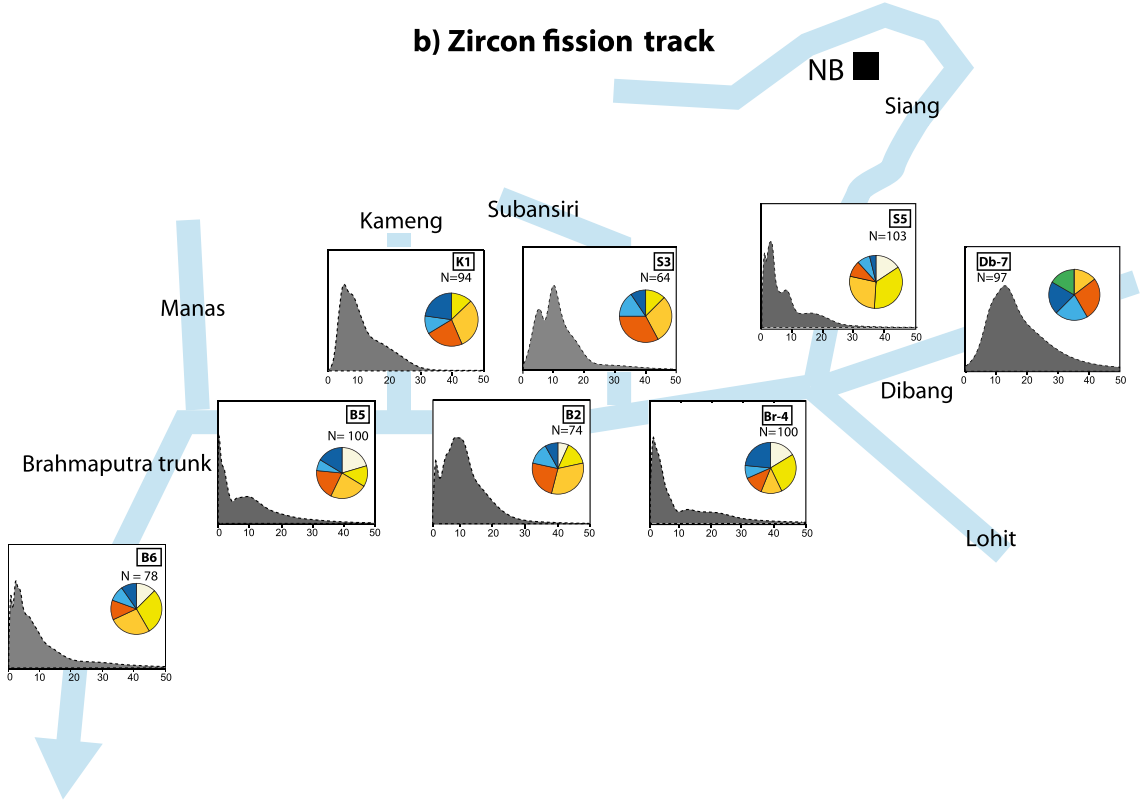

Fig. 3. Probability density plots (PDP) for the measured MAr (a) and ZFT (b) age distributions. All age axes are scaled between 0 and 50 Ma; probabilities are relative and scaled to 1. Samples are positioned along the schematic river courses. Sample code is indicated in top-right of each plot; N = number of grains plotted ($\leq$50 Ma)/number of grains analyzed. The pie charts represent the relative abundances of different age groups (see legend). The PDP are smoother for the ZFT ages compared to the MAr ages due to the lower analytical precision of the single-grain ages.

Table 3
Mineral concentration (%) in modern sand samples of the eastern Himalayan rivers.

River	Site	#samples	#classes	Muscovite	St. deviation	Zircon	St. deviation
Tsangpo	Quxu	1	1	0.00		0.02	
Tsangpo	Shannan	6	1	0.29	0.30	0.08	0.75
Siang	Yingkiong	1	8	1.35		0.01	
Siang	Pasighat	1	1	1.23		0.56	
Brahmaputra	Dibrugarh	1	1	1.55		0.09	
Brahmaputra	Tezpur	2	1	1.89	1.24	0.03	0.03
Brahmaputra	Guwahati	2	1	2.38	2.24	0.12	0.09
Brahmaputra	Yamuna Bridge	8	31	1.38	0.21	0.03	0.04
Manas	at MFT	2	1	2.85	1.65	0.01	0.01
Subansiri	at MBT	3	1	0.53	0.31	0.00	0.03
Dibang	at MBT	1	1	1.08		0.16	
Lohit	at MBT	1	1	0.74		0.00	
Kameng	at MBT	2	1	2.08	1.22	0.03	0.01

results, whereas samples B2 and B6, together with the Subansiri River, show very high values (median values ∼2) with extremely high uncertainties. Overall, the relative erosion-rate values predicted with the ZFT data are more variable than those predicted with the MAr data.

5. Discussion

5.1. Downstream evolution of detrital age distributions

To answer our question of how much the characteristic young age signal from Namche Barwa is preserved or transformed downstream, we look at the evolution of the characteristic <2 Ma age population in the Brahmaputra River samples (Fig. 6). All Siang and Brahmaputra samples present both MAr and ZFT ages <2 Ma, which make up 1–6% of the total age population for MAr and 7–20% for ZFT. The relative importance of this age population decreases downstream, in particular upon entering the Brahmaputra floodplain (sample B4 and further). The most downstream sample (B6) only contains 1% MAr ages <2 Ma, but still has 12% ZFT ages this young.

The signal of <5 Ma MAr ages is similar, encompassing ∼15% of the age distribution in sample S6 and ∼12% in the composite sample S5* (Fig. 5), evolving downstream to 6–9% at B2 and B5. In the Brahmaputra, the proportion of <5 Ma ZFT ages is constant at 40–50% (except in B2, where it is only 22%). However, Himalayan tributaries (except Manas) contribute ∼6–9% MAr ages <5 Ma, and ∼13% ZFT ages in this range. A similar distribution of detrital MAr ages has been reported for the Narayani River catchment in central Nepal (Brewer et al., 2006; Copeland et al., 2015; Ruhl and Hodges, 2005), whereas detrital ZFT data from both Nepal and Arunachal Pradesh consistently show a young age peak with a lag time (i.e. a difference between the thermochronological and depositional ages of the sample) of ∼4 Ma (Bernet et al., 2006; Chirouze et al., 2013). In contrast, these catchments do not contribute MAr or ZFT ages <2 Ma; only 2 grains in the Kameng sample have MAr ages <2 Ma.

The <2 Ma ages thus represent the most robust signal of input from the rapidly exhuming parts of the syntaxis and this signal is present throughout the Brahmaputra River as far as ∼1000 km downstream, despite dilution through input from Himalayan tributaries. The downstream decrease in concentration of <2 Ma ages is less pronounced for ZFT than for MAr; we will discuss possible reasons for this in Section 5.4.

5.2. Erosion-rate patterns and comparison to previous studies

A qualitative comparison of the predicted relative erosion-rate values with the long-term exhumation rates inferred from the detrital age distributions shows first-order agreement between the two, suggesting that present-day erosion rates are consistent with long-term exhumation rates in most catchments. Catchments contributing a high proportion of young ages are also predicted to experience rapid recent erosion (i.e., those along the main Siang River trunk), whereas catchments or sub-catchments with a high proportion of older ages are inferred to be eroding much slower (e.g. the Yarlung–Tsangpo catchments upstream of the syntaxis).

A few exceptions to this pattern may indicate either a recent increase in erosion rates or spurious results: very high relative erosion-rate values are predicted for the most downstream sample (B6) and its tributary the Manas (M9) for both the MAr and ZFT systems, whereas the proportion of young ages in these samples is smaller than in samples located upstream. For the MAr system, this can be related to the relative increase in the 10–20 Ma age bin between samples B5 and B6, which could only have been contributed by the Manas; the large upstream catchment area of the Brahmaputra implies high sediment flux, requiring high erosion rates in the downstream catchments to influence the age distribution downstream. Another example is provided by samples B4 (Brahmaputra) and D7 (Dibang) in the ZFT system: because B4 contains a large proportion of old ages, which the model assumes to have been contributed by the Dibang, relatively high erosion rates are predicted in the latter, compared to the MAr result. In both cases, these discrepancies could correspond to recent increases in erosion rates; relatively high millennial erosion rates have been inferred from detrital ^{10}Be-cosmogenic data from western Bhutan (Portenga et al., 2015), Sikkim (Abrahami et al., 2016), and the eastern Himalayan tributaries (Lupker et al., 2017). However, tests of our mixing model on synthetic data showed a tendency to overestimate relative erosion-rate values in downstream catchments (Braun et al., 2018); the particularly high rates predicted for B6 and M9 may thus be a model artefact. High relative erosion-rate values for the Subansiri catchment are only suggested by the ZFT data and are associated with very large uncertainties; they are not corroborated by the MAr data.

Despite these issues and relatively large uncertainties, the mixing model consistently predicts: (1) a 5-to-100-fold increase in relative erosion-rate values between the Yarlung–Tsangpo and Siang samples, upstream and downstream of Namche Barwa, respectively; (2) erosion rates in the Siang that are 2–10 times those of the southern Himalayan drainage (with the exceptions noted above that we believe are artefacts); (3) low erosion rates in the eastern tributaries of the Brahmaputra (except for the Dibang ZFT sample noted above). We can compare these inferences to previous estimates of erosion rates in the eastern Himalaya (Enkelmann et al., 2011; Garzanti et al., 2004; Singh and France-Lanord, 2002; Stewart et al., 2008). These used sediment geochemistry, petrography, and thermochronology data from the Brahmaputra and its tributaries to estimate that 35–70% of the sediment flux of the Brahmaputra where it enters the foreland (Fig. 1) was sourced

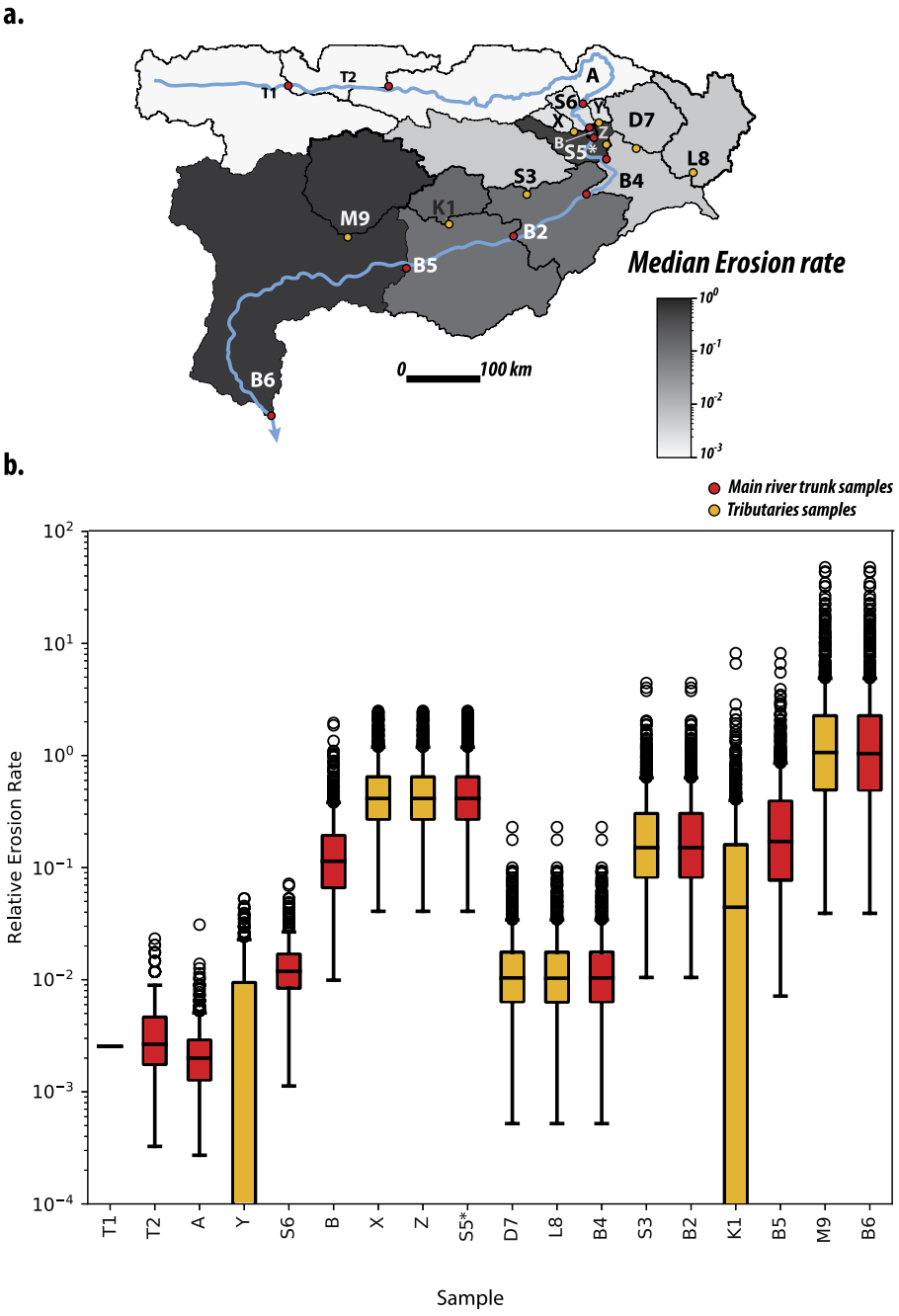

Fig. 4. Present-day relative erosion-rate pattern in the eastern Himalaya as predicted by linear inversion of the MAr ages. The map (a) shows catchments included in the model, shaded according to the predicted median relative erosion rates. Samples (catchment outlets) are indicated by orange dots for the tributaries and red dots for the main trunk; blue line indicates course of main Yarlung–Tsangpo–Siang–Brahmaputra River. Box-plot (b) shows variance of predicted relative erosion rates from the bootstrapping analysis for the different catchments, as a function of downstream distance of the sampling site along the Yarlung–Tsangpo–Siang–Brahmaputra River. Horizontal line shows median rate, box delimits 25–75 percentile and is colored orange for tributaries and red for main trunk samples, bar extends to mean ±1 standard deviation, and individual outliers are indicated by dots.

from Namche Barwa, which only makes up 3–8% of the upstream drainage area (depending on its exact definition), requiring the erosion rate in the massif to be 6–75 times the average upstream erosion rate. These estimates, although widely varying, are broadly consistent with our inferences.

More recently, Lupker et al. (2017) conducted a study that was very similar in design to ours, but used detrital ^{10}Be-cosmogenic data to infer erosion-rate patterns. These authors reported erosion rates $\leq$0.2 mm yr^{-1} for the Yarlung–Tsangpo catchments upstream of the syntaxis, 2–5 mm yr^{-1} for the syntaxis region (4–28 mm yr^{-1} when assuming that rapid erosion is concentrated in the Namche Barwa massif), and 0.7–1.1 mm yr^{-1} for the southern Himalayan catchments, consistent with our estimates. There are some remarkable consistencies between our study and that of Lupker et al. (2017), such as the intriguingly low erosion rates suggested by the Pasighat sample for the ZFT target mineral, but also some contrasting results. In particular, our Pasighat sample implies high relative erosion rates for the MAr system, in line with previous detrital studies (e.g., Enkelmann et al., 2011; Lang et al., 2016). Interestingly, the highest erosion rates from the MAr system are predicted for catchments south of the Namche Barwa massif, whereas the ZFT data suggest the highest rates for tributaries di-

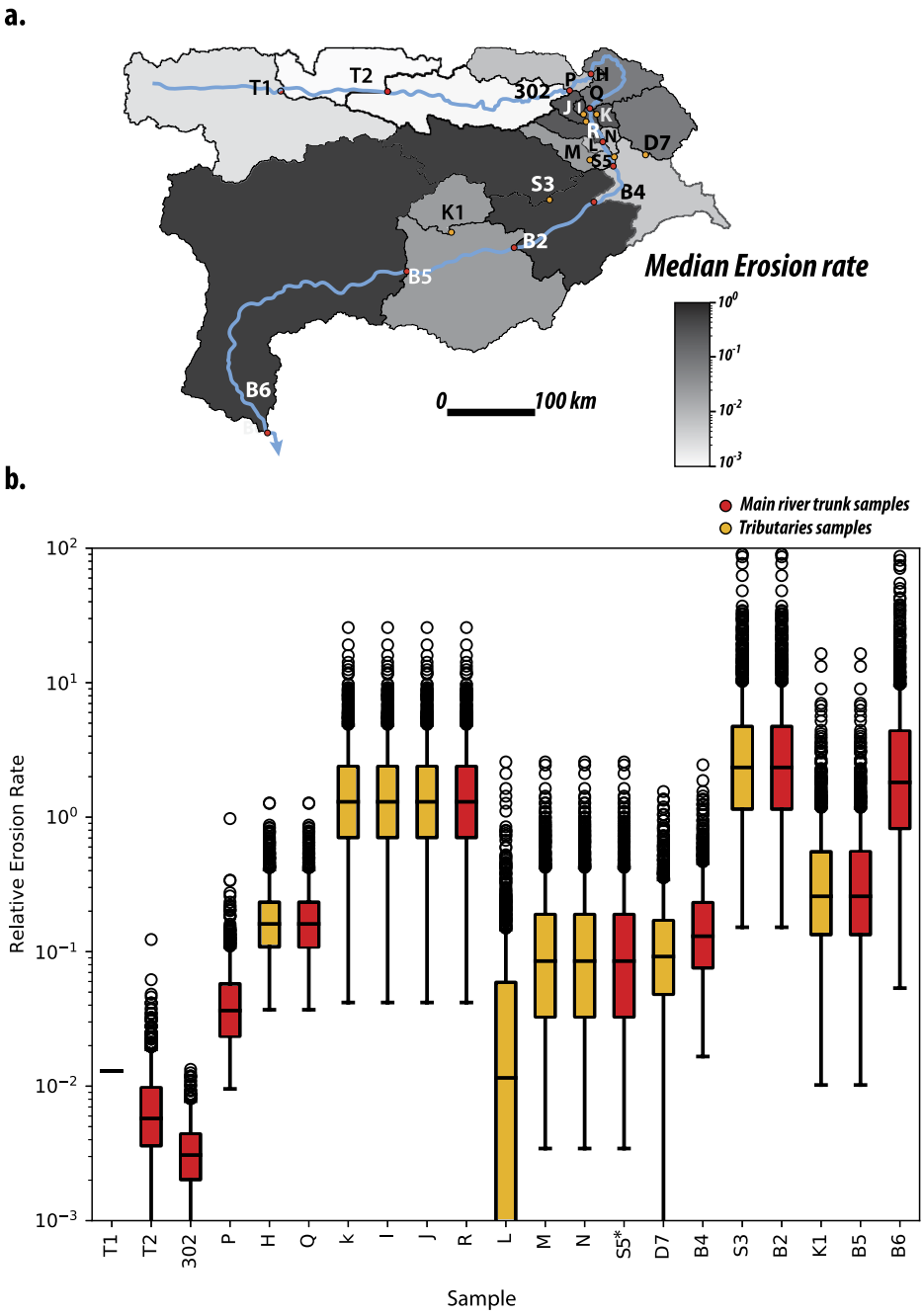

Fig. 5. Present-day relative erosion-rate pattern in the eastern Himalaya as predicted by linear inversion of the ZFT ages. See Fig. 4 legend for explanation. Note that some tributaries (Lohit, Manas) were not sampled for ZFT and are included in the catchment area of the downstream trunk sample.

rectly draining the massif and lower rates to the south. Lupker et al. (2017) observed a similar behavior to our MAr data and suggested this was due to grain abrasion and a grain-size bias: grains eroded from the Namche Barwa massif are only abraded to the size collected during sampling several tens of km downstream and are therefore missed in the most proximal samples.

Most of our data (except the Dibang ZFT data) suggest low erosion rates in the eastern tributaries of the Brahmaputra, in contrast to Lupker et al. (2017), who reported some of the highest erosion rates in their study (2.0–3.4 mm yr^{-1}) from these rivers. Our MAr and ZFT data suggest contrasting and largely unconstrained erosion rates for the Subansiri catchment, for which Lupker et al. (2017) reported very high erosion rates of 2.1–4.4 mm yr^{-1}. Clearly, more data is required from these remote eastern Himalayan catchments to fully constrain their erosion dynamics.

5.3. Potential sources of error

All of the above methods of inferring the spatial pattern of present-day erosion rates, including ours, suffer from significant uncertainties. Erosion rates predicted by our mixing model are sensitive to estimated concentrations of the target mineral in the eroded rocks (Braun et al., 2018; see also Appendix B; Eqs. (B8), (B9)), which may vary widely and are challenging to measure (Malusà et al., 2016). We have used petrographic and heavy-mineral analyses on river sands to constrain target-mineral concentrations in our catchments; the results show standard deviations

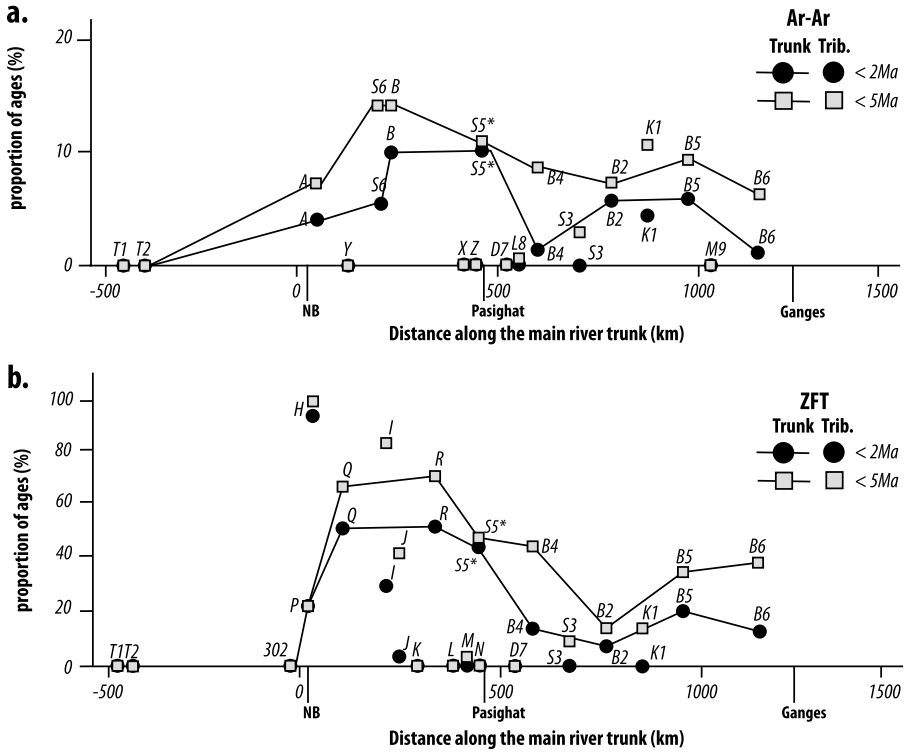

Fig. 6. (a) Proportion of MAr ages <2 Ma (black circles) and <5 Ma (gray squares) downstream. (b) Proportion of ZFT ages <2 Ma (black circles) and <5 Ma (gray squares) downstream. In both plots, trunk-stream samples are connected by solid lines; tributary samples are plotted individually. Namche Barwa massif (NB), Pasighat (where the river enters the foreland and becomes the Brahmaputra) and Ganges confluence are indicated on the *x*-axes of each plot.

of up to >100% of the mean, both within and between samples (Table 3). The resolution with which the age data themselves can constrain the erosion rates was assessed by our bootstrapping analysis; the results show uncertainties ≥60%, increasing to values of up to 200% in the most downstream samples. Therefore, our method provides only a relatively coarse view of the pattern of erosion rates, but the order-of-magnitude variations in relative erosion rates inferred from the data are robust with respect to the internal uncertainty.

Another issue concerns the representativeness and reproducibility of the data (i.e. the thermochronological age distributions themselves), which can be affected by stochastic sediment production and transport processes such as landslides or mega-floods (Lang et al., 2013; Larsen and Montgomery, 2012; Whipp et al., 2016). A rigorous assessment of reproducibility would require resampling at different times and redoing the experiment. We can do something similar by comparing the data from our sample S5 with those published by Stewart et al. (2008), Enkelmann et al. (2011), Bracciali et al. (2016), and Lang et al. (2016) for samples collected at the same location. Both the previously published MAr (Bracciali et al., 2016; Lang et al., 2016) and ZFT (Stewart et al., 2008; Enkelmann et al., 2011) age populations contain a larger proportion of young grains than our sample S5, despite apparently similar analytical procedures. The reason for this difference is not clear; it may reflect a limit to the reproducibility of these samples, or result from the criteria used to count specific zircon grains for fission-track analyses and to accept or reject MAr results. This discrepancy calls for further standardization of methods or at least more complete description of laboratory procedures in detrital studies. It also underscores the challenge of obtaining reproducible results for very young (≤~1 Ma) grains, at the limits of the current resolution for both the ZFT and MAr methods. However, we combined these samples in the mixing model used to extract erosion rates, thereby averaging potential biases that may have existed between the datasets.

5.4. Controls on downstream changes in age distributions

Finally, we aim to assess what processes (dilution from downstream tributaries, chemical and mechanical breakdown of target minerals, hydraulic sorting) control the downstream evolution of age distributions. We can predict the expected effect of dilution using a simple sediment-flux calculation (Chirouze et al., 2015), assuming no significant differences in abundance of mica and zircon in the different contributing units, as suggested by our petrographic data (Table 3).

Based on bedrock thermochronology data from the literature (Fig. 2 b, c), we mapped out the areas exposing <2 Ma and <5 Ma ages for the biotite $^{40}Ar/^{39}Ar$ (BAr), ZFT and zircon (U–Th)/He (ZHe) systems (Supplementary Table C). By multiplying each of the computed areas (km^2) with the inferred erosion rates ($mm\,yr^{-1}$), we predict the expected yearly sediment flux ($m^3\,yr^{-1}$ or, after multiplying by rock density, $Mt\,yr^{-1}$) from these areas (Supplementary Table C). We then compare this sediment flux with the total predicted sediment flux at the locations of samples S5 and B6, calculated in a similar manner. We take the erosion rates reported by Lupker et al. (2017): 2–5 $mm\,yr^{-1}$ for the NB massif, 0.1–0.2 $mm\,yr^{-1}$ for the Yarlung–Tsangpo drainage upstream of the NB and 0.7–1.1 $mm\,yr^{-1}$ for the southern Himalayan tributaries. We estimate the total sediment flux at Pasighat to be 397–583 $Mt\,yr^{-1}$. This is significantly higher than the measured modern-day (1955–1979) value of 233 ± 92 $Mt\,yr^{-1}$ (Goswami, 1985); Lupker et al. (2017) discuss possible reasons for this discrepancy. From our calculations, we expect 18 ± 4% of the ZFT ages and 11 ± 2% of the MAr ages in the Pasighat sample to be <2 Ma. These numbers are somewhat higher than the proportions we measured (10% of ZFT ages and 5% of MAr ages <2 Ma in sample S5), suggesting that we may be missing some of the youngest ages in this sample. The estimate for MAr is consistent with the combined sample we used in the mixture model (11% MAr ages <2 Ma), whereas for ZFT it is lower than the proportion

of <2 Ma ages in the combined sample (38%). For the most downstream sample B6, these proportions are expected to decrease to 10 ± 2% for ZFT and 6 ± 1% for MAr, in line with the observations for ZFT (11%) but significantly higher than the observed concentration of young MAr ages (1%). We note, however, that given the lack of bedrock MAr ages and the relative scarcity of ZFT ages in the NB massif, the inferred source areas are based on the BAr and ZFT + ZHe systems and are therefore somewhat overestimated, because the closure temperatures of the BAr and ZHe systems are somewhat lower than those of the MAr and ZFT systems, respectively (Reiners and Brandon, 2006). The above estimates of the contribution to the sediment flux are therefore upper limits.

The above estimates suggest that the observed downstream decrease in the proportion of young ZFT ages derived from Namche Barwa can be explained by dilution from input of Himalayan tributaries to the Brahmaputra. For the MAr system, the decrease is too strong to be explained by dilution alone, except if our petrographic data underestimate the concentration of white mica in the southern Himalayan catchments compared to the Namche Barwa. However, our (admittedly sparse) petrographic data do not support large differences in concentration of white mica between the different catchments. Moreover, such underestimations would have been reflected in our mixing model by distinctively higher relative erosion rates in these catchments for MAr than for ZFT, which are not predicted by the model.

Another possibility is that either mechanical or chemical breakdown or hydraulic sorting effects, which can have a major influence on the mineralogical and chemical composition of sediments (Garçon et al., 2013; Garzanti et al., 2010), affect micas more strongly than zircons in the Brahmaputra River. Zircons are transported as bedload, whereas phyllosilicates constitute the bulk of the suspended load of the Brahmaputra (Garzanti et al., 2010, 2011). Mechanical breakdown is inefficient in suspended sediment, whereas chemical weathering does not affect Brahmaputra river sediments strongly because of the high transport rates (Garzanti et al., 2004).

Hydraulic sorting effects would be expected to affect the ZFT signal differently from the MAr signal, due to the different transport modes of these two minerals. Zircons can be concentrated in placer lag deposits by selective entrainment. However, this local process is probably not very effective in the long term, because fluvial bars in the Brahmaputra are reworked annually during monsoon floods. In contrast, the low settling velocity of micas makes them very susceptible to sequestration in overbank and floodplain deposits through winnowing during floods. This different susceptibility to hydraulic sorting effects may explain why the MAr signal is more strongly transformed downstream than the ZFT signal, and more strongly than expected from downstream dilution alone. However, although it is transformed, the signal of syntaxial denudation is retained in all of our samples, collected up to 1000 km downstream of the syntaxis.

5.5. Implications for detrital thermochronology records

As the syntaxial age signal endures downstream, it should be visible in sedimentary deposits in the foreland and is diagnostic of rapid exhumation in the Namche Barwa massif. Such young Mar and ZFT ages, associated with short lag times, are encountered in sediments deposited around 5–6 Ma in proximal sites (Siwaliks in the Pasighat area; Govin, 2017; Lang et al., 2016) but only in sediments <2 Ma in the more distal Surma Basin in Bangladesh (Bracciali et al., 2016), whereas Chirouze et al. (2013) did not encounter such ages at all in the Kameng River section of western Arunachal Pradesh. Our analysis suggests that these discrepancies cannot be explained by modification of the detrital thermochronology signal downstream. However, if the region of rapid exhumation has grown through time (as argued, for instance, by Seward and Burg, 2008; but note the opposite viewpoint expressed by Zeitler et al., 2014), the dilution effect could make the signal challenging to detect in earlier distal records, since the initial flux of young-age grains may have been significantly smaller than at present. Alternatively, these differences may result from potential drainage reorganization in the foreland downstream of the syntaxis, which could affect the more distal sites. Note also that we assessed the effect of hydraulic sorting for the Brahmaputra down to the confluence with the Ganga River only; as the river enters its depositional realm downstream from here, these effects may become significantly more important (Garçon et al., 2013; Garzanti et al., 2010). The most directly interpretable record of syntaxial exhumation would thus be obtained in proximal detrital thermochronology records, such as those collected by Lang et al. (2016) and Govin (2017).

6. Conclusions

We have quantified the evolution of the detrital thermochronological MAr and ZFT age signatures downstream of the eastern Himalayan syntaxis, along the Brahmaputra River and its tributaries. Our data show that the characteristic signal of young (<2 Ma) ages originating from the Namche Barwa massif is preserved up to at least 1000 km downstream. This signal can thus be used in the sedimentary record as indicating rapid exhumation in the syntaxis.

We have used a linear inversion of the age distributions to map out patterns of relative erosion-rate values in the sampled catchments. The target-mineral concentration in the rocks eroded from each catchment was estimated from sand petrography and heavy-mineral analyses. Although our approach is associated with significant errors, robust predictions of the inversion are: (1) a 5-to-100-fold increase in erosion rates between the Yarlung–Tsangpo and Siang samples, upstream and downstream of Namche Barwa, respectively; (2) erosion rates in the southern flank of the Himalaya that are 2–10 times lower than in the Siang river; (3) low erosion rates in the eastern tributaries of the Brahmaputra. These inferences are in overall accord with previous estimates of erosion rates in the eastern Himalaya, except for the eastern tributaries, the erosional regime of which remains incompletely understood.

A simple sediment-budget calculation suggests that the evolution of the detrital ZFT signal downstream of Namche Barwa can be explained by dilution from Himalayan tributaries. The MAr signal, in contrast, appears affected by hydraulic sorting effects, in particular winnowing and selective sequestration in the floodplain during monsoon floods. Such variable behavior of target minerals for detrital thermochronology studies should be taken into account when interpreting the detrital record of Himalayan exhumation.

Acknowledgements

This work is part of the iTECC (investigating Tectonics-Erosion-Climate Coupling) ITN, supported by the EU FP7 (grant agreement no. 316966). ISTerre is part of Labex OSUG@2020 (ANR10 LABX56). Natalie Vögeli, Gwladys Govin, and Katu Bage provided support during fieldwork. Roel van Elsas is acknowledged for help during mineral separation and Onno Postma for help in the $^{40}Ar/^{39}Ar$ laboratory. Mélanie Balvay helped with ZFT analyses, and Klaudia Kuiper with the treatment and interpretation of MAr data. Comments by two anonymous reviewers and Peter Zeitler helped to significantly improve previous versions of this manuscript. This manuscript is the dedicated to the memory of our beloved friend and colleague Gwladys Govin.

Appendix. Supplementary material

Supplementary material related to this article can be found online at https://doi.org/10.1016/j.epsl.2018.07.019.

References

Abrahami, R., van der Beek, P., Huyghe, P., Hardwick, E., Carcaillet, J., 2016. Decoupling of long-term exhumation and short-term erosion rates in the Sikkim Himalaya. Earth Planet. Sci. Lett. 433, 76–88. https://doi.org/10.1016/j.epsl.2015.10.039.

Acharyya, S.K., 2007. Evolution of the Himalayan Paleogene foreland basin, influence of its litho-packet on the formation of thrust-related domes and windows in the Eastern Himalayas – a review. J. Asian Earth Sci. 31, 1–17. https://doi.org/10.1016/j.jseaes.2007.03.007.

Adams, B.A., Hodges, K.V., Whipple, K.X., Ehlers, T.A., van Soest, M.C., Wartho, J., 2015. Constraints on the tectonic and landscape evolution of the Bhutan Himalaya from thermochronometry. Tectonics 34, 1329–1347. https://doi.org/10.1002/2015TC003853.

Adlakha, V., Lang, K.A., Patel, R.C., Lal, N., Huntington, K.W., 2013. Rapid long-term erosion in the rain shadow of the Shillong Plateau, Eastern Himalaya. Tectonophysics 582, 76–83. https://doi.org/10.1016/j.tecto.2012.09.022.

Bendick, R., Ehlers, T.A., 2014. Extreme localized exhumation at syntaxes initiated by subduction geometry. Geophys. Res. Lett. 41, 5861–5867. https://doi.org/10.1002/2014GL061026.

Bernet, M., Garver, J.I., 2005. Fission-track analysis of detrital zircon. Rev. Mineral. Geochem. 58, 205–237. https://doi.org/10.2138/rmg.2005.58.8.

Bernet, M., Brandon, M.T., Garver, J.I., Molitor, B., 2004. Downstream changes of Alpine zircon fission-track ages in the Rhône and Rhine rivers. J. Sediment. Res. 74, 82–94.

Bernet, M., van der Beek, P., Pik, R., Huyghe, P., Mugnier, J.-L., Labrin, E., Szulc, A., 2006. Miocene to Recent exhumation of the central Himalaya determined from combined detrital zircon fission-track and U/Pb analysis of Siwalik sediments, western Nepal. Basin Res. 18, 393–412. https://doi.org/10.1111/j.1365-2117.2006.00303.x.

Biswas, S., Coutand, I., Grujic, D., Hager, C., Stockli, D., Grasemann, B., 2007. Exhumation and uplift of the Shillong plateau and its influence on the eastern Himalayas: new constraints from apatite and zircon (U–Th–[Sm])/He and apatite fission track analyses. Tectonics 26, TC6013. https://doi.org/10.1029/2007TC002125.

Bracciali, L., Najman, Y., Parrish, R.R., Akhter, S.H., Millar, I., 2015. The Brahmaputra tale of tectonics and erosion: Early Miocene river capture in the Eastern Himalaya. Earth Planet. Sci. Lett. 415, 25–37. https://doi.org/10.1016/j.epsl.2015.01.022.

Bracciali, L., Parrish, R.R., Najman, Y., Smye, A., Carter, A., Wijbrans, J.R., 2016. Plio-Pleistocene exhumation of the eastern Himalayan syntaxis and its domal "pop-up". Earth-Sci. Rev. 160, 350–385. https://doi.org/10.1016/j.earscirev.2016.07.010.

Braun, J., Gemignani, L., van der Beek, P., 2018. Extracting information on the spatial variability in erosion rate stored in detrital cooling age distributions in river sands. Earth Surf. Dyn. 6, 257–270. https://doi.org/10.5194/esurf-6-257-2018.

Brewer, I.D., Burbank, D.W., Hodges, K.V., 2006. Downstream development of a detrital cooling-age signal: insights from $^{40}Ar/^{39}Ar$ muscovite thermochronology in the Nepalese Himalaya. Spec. Pap., Geol. Soc. Am. 398, 321–338. https://doi.org/10.1130/2006.2398(20).

Burg, J.-P., Davy, P., Nievergelt, P., Oberli, F., Seward, D., Diao, Z., Meier, M., 1997. Exhumation during crustal folding in the Namche–Barwa syntaxis. Terra Nova 9, 53–56. https://doi.org/10.1111/j.1365-3121.1997.tb00001.x.

Carrapa, B., Robert, X., DeCelles, P.G., Orme, D.A., Thomson, S.N., Schoenbohm, L.M., 2016. Asymmetric exhumation of the Mount Everest region: implications for the tectono-topographic evolution of the Himalaya. Geology 44, 611–614. https://doi.org/10.1130/G37756.1.

Chirouze, F., Huyghe, P., van der Beek, P., Chauvel, C., Chakraborty, T., Dupont-Nivet, G., Bernet, M., 2013. Tectonics, exhumation, and drainage evolution of the eastern Himalaya since 13 Ma from detrital geochemistry and thermochronology, Kameng River Section, Arunachal Pradesh. Geol. Soc. Am. Bull. 125, 523–538. https://doi.org/10.1130/B30697.1.

Chirouze, F., Huyghe, P., Chauvel, C., van der Beek, P., Bernet, M., Mugnier, J.-L., 2015. Stable drainage pattern and variable exhumation in the western Himalaya since the middle Miocene. J. Geol. 123, 1–20. https://doi.org/10.1086/679305.

Cina, S.E., Yin, A., Grove, M., Dubey, C.S., Shukla, D.P., Lovera, O.M., Kelty, T.K., Gehrels, G.E., Foster, D.A., 2009. Gangdese arc detritus within the eastern Himalayan Neogene foreland basin: implications for the Neogene evolution of the Yalu–Brahmaputra River system. Earth Planet. Sci. Lett. 285, 150–162. https://doi.org/10.1016/j.epsl.2009.06.005.

Clark, M.K., Bilham, R., 2008. Miocene rise of the Shillong Plateau and the beginning of the end for the Eastern Himalaya. Earth Planet. Sci. Lett. 269, 336–350. https://doi.org/10.1016/j.epsl.2008.01.045.

Clark, M.K., Schoenbohm, L.M., Royden, L.H., Whipple, K.X., Burchfiel, B.C., Zhang, X., Tang, W., Wang, E., Chen, L., 2004. Surface uplift, tectonics, and erosion of eastern Tibet from large-scale drainage patterns. Tectonics 23, TC1006. https://doi.org/10.1029/2002TC001402.

Copeland, P., Harrison, T.M., Yun, P., Kidd, W., 1995. Thermal evolution of the Gangdese batholith, southern Tibet: a history of episodic unroofing. Tectonics 14, 223–236.

Copeland, P., Bertrand, G., France-Lanord, C., Sundell, K., 2015. $^{40}Ar/^{39}Ar$ ages of muscovites from modern Himalayan rivers: Himalayan evolution and the relative contribution of tectonics and climate. Geosphere 11, 1837–1859. https://doi.org/10.1130/GES01154.1.

Coutand, I., Whipp, D.M., Grujic, D., Bernet, M., Fellin, M.G., Bookhagen, B., Landry, K.R., Ghalley, S.K., Duncan, C., 2014. Geometry and kinematics of the Main Himalayan Thrust and Neogene crustal exhumation in the Bhutanese Himalaya derived from inversion of multithermochronologic data. J. Geophys. Res. 119, 1446–1481. https://doi.org/10.1002/2013JB010891.

DeCelles, P.G., Carrapa, B., Gehrels, G.E., Chakraborty, T., Ghosh, P., 2016. Along-strike continuity of structure, stratigraphy, and kinematic history in the Himalayan thrust belt: the view from Northeastern India. Tectonics 35, 2995–3027. https://doi.org/10.1002/2016TC004298.

Enkelmann, E., Ehlers, T.A., Zeitler, P.K., Hallet, B., 2011. Denudation of the Namche Barwa antiform, eastern Himalaya. Earth Planet. Sci. Lett. 307, 323–333. https://doi.org/10.1016/j.epsl.2011.05.004.

Finnegan, N.J., Hallet, B., Montgomery, D.R., Zeitler, P.K., Stone, J.O., Anders, A.M., Yuping, L., 2008. Coupling of rock uplift and river incision in the Namche Barwa–Gyala Peri massif, Tibet. Geol. Soc. Am. Bull. 120, 142–155. https://doi.org/10.1130/B26224.1.

Gansser, A., 1980. The significance of the Himalayan suture zone. Tectonophysics 62, 37–52.

Garçon, M., Chauvel, C., France-Lanord, C., Huyghe, P., Lavé, J., 2013. Continental sedimentary processes decouple Nd and Hf isotopes. Geochim. Cosmochim. Acta 121, 177–195. https://doi.org/10.1016/j.gca.2013.07.027.

Garzanti, E., Vezzoli, G., Andò, S., France-Lanord, C., Singh, S.K., Foster, G., 2004. Sand petrology and focused erosion in collision orogens: the Brahmaputra case. Earth Planet. Sci. Lett. 220, 157–174. https://doi.org/10.1016/S0012-821X(04)00035-4.

Garzanti, E., Andò, S., France-Lanord, C., Vezzoli, G., Censi, P., Galy, V., Najman, Y., 2010. Mineralogical and chemical variability of fluvial sediments 1. Bedload sand (Ganga–Brahmaputra, Bangladesh). Earth Planet. Sci. Lett. 299, 368–381. https://doi.org/10.1016/j.epsl.2010.09.017.

Garzanti, E., Andò, S., France-Lanord, C., Censi, P., Vignola, P., Galy, V., Lupker, M., 2011. Mineralogical and chemical variability of fluvial sediments 2. Suspended-load silt (Ganga–Brahmaputra, Bangladesh). Earth Planet. Sci. Lett. 302, 107–120. https://doi.org/10.1016/j.epsl.2010.11.043.

Gemignani, L., Sun, X., Braun, J., van Gerve, T.D., Wijbrans, J.R., 2017. A new detrital mica $^{40}Ar/^{39}Ar$ dating approach for provenance and exhumation of the Eastern Alps. Tectonics 36, 1521–1537. https://doi.org/10.1002/2017TC004483.

Glotzbach, C., van der Beek, P., Carcaillet, J., Delunel, R., 2013. Deciphering the driving forces of erosion rates on millennial to million-year timescales in glacially impacted landscapes: an example from the Western Alps. J. Geophys. Res. 118, 1491–1515. https://doi.org/10.1002/jgrf.20107.

Goswami, D.C., 1985. Brahmaputra River, Assam, India: physiography, basin denudation, and channel aggradation. Water Resour. Res. 21, 959–978. https://doi.org/10.1029/WR021i007p00959.

Govin, G., 2017. Tectonic-Erosion Interactions: Insights from the Paleo-Drainage of the Brahmaputra River. PhD thesis. Lancaster University, U.K. 331 pp.

Govin, G., Najman, Y.M.R., Copley, A., Millar, I., van der Beek, P., Huyghe, P., Grujic, D., Davenport, J., 2018. Timing and mechanism of the rise of the Shillong Plateau in the Himalayan foreland. Geology 46, 279–282. https://doi.org/10.1130/g39864.1.

Grujic, D., Coutand, I., Bookhagen, B., Bonnet, S., Blythe, A., Duncan, C., 2006. Climatic forcing of erosion, landscape, and tectonics in the Bhutan Himalayas. Geology 34, 801–814. https://doi.org/10.1130/G22648.1.

Hallet, B., Molnar, P., 2001. Distorted drainage basins as markers of crustal strain East of the Himalaya. J. Geophys. Res. 106, 13697–13709. https://doi.org/10.1029/2000JB900335.

Haproff, P.J., Zuza, A.V., Yin, A., 2018. West-directed thrusting south of the eastern Himalayan syntaxis indicates clockwise crustal flow at the indenter corner during the India–Asia collision. Tectonophysics 722, 277–285. https://doi.org/10.1016/j.tecto.2017.11.001.

Hodges, K.V., 2000. Tectonics of the Himalaya and southern Tibet from two perspectives. Geol. Soc. Am. Bull. 112, 324–350. https://doi.org/10.1130/0016-7606(2000)112<324:TOTHAS>2.0.CO;2.

Hodges, K.V., Ruhl, K.W., Wobus, C.W., Pringle, M.S., 2005. $^{40}Ar/^{39}Ar$ thermochronology of detrital minerals. Rev. Mineral. Geochem. 58, 239–257. https://doi.org/10.2138/rmg.2005.58.9.

Kellett, D.A., Grujic, D., Coutand, I., Cottle, J., Mukul, M., 2013. The South Tibetan detachment system facilitates ultra rapid cooling of granulite-facies rocks in Sikkim Himalaya. Tectonics 32, 252–270. https://doi.org/10.1002/tect.20014.

King, G.E., Herman, F., Guralnik, B., 2016. Northward migration of the eastern Himalayan syntaxis revealed by OSL thermochronometry. Science 353, 800–804. https://doi.org/10.1126/science.aaf2637.

Lang, K.A., Huntington, K.W., 2014. Antecedence of the Yarlung–Siang–Brahmaputra River, eastern Himalaya. Earth Planet. Sci. Lett. 397, 145–158. https://doi.org/10.1016/j.epsl.2014.04.026.

Lang, K.A., Huntington, K.W., Montgomery, D.R., 2013. Erosion of the Tsangpo Gorge by megafloods, Eastern Himalaya. Geology 41, 1003–1006. https://doi.org/10.1130/G34693.1.

Lang, K.A., Huntington, K.W., Burmester, R., Housen, B., 2016. Rapid exhumation of the eastern Himalayan syntaxis since the late Miocene. Geol. Soc. Am. Bull. 128, 1403–1422. https://doi.org/10.1130/B31419.1.

Larsen, I.J., Montgomery, D.R., 2012. Landslide erosion coupled to tectonics and river incision. Nat. Geosci. 5, 468–473. https://doi.org/10.1038/ngeo1479.

Li, G., Tian, Y., Kohn, B.P., Sandiford, M., Xu, Z., Cai, Z., 2015. Cenozoic low temperature cooling history of the Northern Tethyan Himalaya in Zedang, SE Tibet and its implications. Tectonophysics 643, 80–93. https://doi.org/10.1016/j.tecto.2014.12.014.

Li, G., Kohn, B., Sandiford, M., Xu, Z., Tian, Y., Seiler, C., 2016. Synorogenic morphotectonic evolution of the Gangdese batholith, South Tibet: insights from low-temperature thermochronology. Geochem. Geophys. Geosyst. 17, 101–112. https://doi.org/10.1002/2015gc006047.

Long, S.P., McQuarrie, N., Tobgay, T., Coutand, I., Cooper, F.J., Reiners, P.W., Wartho, J.-A., Hodges, K.V., 2012. Variable shortening rates in the eastern Himalayan thrust belt, Bhutan: insights from multiple thermochronologic and geochronologic data sets tied to kinematic reconstructions. Tectonics 31, TC5004. https://doi.org/10.1029/2012TC003155.

Lupker, M., Lavé, J., France-Lanord, C., Christl, M., Bourlès, D., Carcaillet, J., Maden, C., Wieler, R., Rahman, M., Bezbaruah, D., Xiaohan, L., 2017. ^{10}Be systematics in the Tsangpo–Brahmaputra catchment: the cosmogenic nuclide legacy of the eastern Himalayan syntaxis. Earth Surf. Dyn. 5, 429–449. https://doi.org/10.5194/esurf-5-429-2017.

Malusà, M.G., Resentini, A., Garzanti, E., 2016. Hydraulic sorting and mineral fertility bias in detrital geochronology. Gondwana Res. 31, 1–19. https://doi.org/10.1016/j.gr.2015.09.002.

Misra, D.K., 2009. Litho-tectonic sequence and their regional correlation along the Lohit and Dibang valleys, eastern Arunachal Pradesh. J. Geol. Soc. India 73, 213–219.

Portenga, E.W., Bierman, P.R., Duncan, C., Corbett, L.B., Kehrwald, N.M., Rood, D.H., 2015. Erosion rates of the Bhutanese Himalaya determined using in situ-produced ^{10}Be. Geomorphology 233, 112–126. https://doi.org/10.1016/j.geomorph.2014.09.027.

Reiners, P.W., Brandon, M.T., 2006. Using thermochronology to understand orogenic erosion. Annu. Rev. Earth Planet. Sci. 34, 419–466. https://doi.org/10.1007/978-3-540-48684-8.

Ruhl, K.W., Hodges, K.V., 2005. The use of detrital mineral cooling ages to evaluate steady state assumptions in active orogens: an example from the central Nepalese Himalaya. Tectonics 24, TC4015. https://doi.org/10.1029/2004TC001712.

Salvi, D., Mathew, G., Kohn, B., 2017. Rapid exhumation of the upper Siang Valley, Arunachal Himalaya since the Pliocene. Geomorphology 284, 238–249. https://doi.org/10.1016/j.geomorph.2016.09.032.

Schultz, M.H., Hodges, K.V., Ehlers, T.A., van Soest, M., Wartho, J.-A., 2017. Thermochronologic constraints on the slip history of the South Tibetan detachment system in the Everest region, southern Tibet. Earth Planet. Sci. Lett. 459, 105–117. https://doi.org/10.1016/j.epsl.2016.11.022.

Seward, D., Burg, J.-P., 2008. Growth of the Namche Barwa Syntaxis and associated evolution of the Tsangpo Gorge: constraints from structural and thermochronological data. Tectonophysics 451, 282–289. https://doi.org/10.1016/j.tecto.2007.11.057.

Singh, S.K., France-Lanord, C., 2002. Tracing the distribution of erosion in the Brahmaputra watershed from isotopic compositions of stream sediments. Earth Planet. Sci. Lett. 202, 645–662. https://doi.org/10.1016/S0012-821X(02)00822-1.

Stewart, R.J., Brandon, M.T., 2004. Detrital-zircon fission-track ages for the "Hoh Formation": implications for late Cenozoic evolution of the Cascadia subduction wedge. Geol. Soc. Am. Bull. 116, 60–75. https://doi.org/10.1130/B22101.1.

Stewart, R.J., Hallet, B., Zeitler, P.K., Malloy, M.A., Allen, C.M., Trippett, D., 2008. Brahmaputra sediment flux dominated by highly localized rapid erosion from the easternmost Himalaya. Geology 36, 711–739. https://doi.org/10.1130/G24890A.1.

Stock, G.M., Ehlers, T.A., Farley, K.A., 2006. Where does sediment come from? Quantifying catchment erosion with detrital apatite (U–Th)/He thermochronometry. Geology 34, 725–728. https://doi.org/10.1130/G22592.1.

Stüwe, K., Foster, D., 2001. ^{40}Ar/^{39}Ar, pressure, temperature and fission track constraints on the age and nature of metamorphism around the main central thrust in the eastern Bhutan Himalaya. J. Asian Earth Sci. 19, 85–95. https://doi.org/10.1016/S1367-9120(00)00018-3.

Vermeesch, P., 2012. On the visualisation of detrital age distributions. Chem. Geol. 312–313, 190–194. https://doi.org/10.1016/j.chemgeo.2012.04.021.

Wang, P., Scherler, D., Liu-Zeng, J., Mey, J., Avouac, J.P., 2014. Tectonic control of Yarlung Tsangpo Gorge revealed by a buried canyon in Southern Tibet. Science 346, 978–981. https://doi.org/10.1126/science.1259041.

Whipp, D.M., Coutand, I., Bookhagen, B., Grujic, D., 2016. Interpreting records of tectonic and erosional processes using detrital thermochronology: an example from the Bhutan Himalaya. AGU Fall Meeting abstract, T42B-05.

Yin, A., Harrison, T.M., 2000. Geologic evolution of the Himalayan–Tibetan orogen. Annu. Rev. Earth Planet. Sci. 28, 211–280. https://doi.org/10.1146/annurev.earth.28.1.211.

Yin, A., Harrison, T.M., Murphy, M.A., Grove, M., Nie, S., Ryerson, F.J., Feng, W.X., Le, C.Z., 1999. Tertiary deformation history of southeastern and southwestern Tibet during the Indo-Asian collision. Geol. Soc. Am. Bull. 111, 1644–1664. https://doi.org/10.1130/0016-7606(1999)111<1644:TDHOSA>2.3.CO;2.

Yin, A., Dubey, C.S., Kelty, T.K., Webb, A.A.G., Harrison, T.M., Chou, C.Y., Celerier, J., 2010. Geologic correlation of the Himalayan orogen and Indian craton: Part 2. Structural geology, geochronology, and tectonic evolution of the Eastern Himalaya. Geol. Soc. Am. Bull. 122, 360–395. https://doi.org/10.1130/B26461.1.

Zeitler, P.K., Meltzer, A.S., Koons, P.O., Craw, D., Hallet, B., Chamberlain, C.P., Kidd, W.S.F., Park, S.K., Seeber, L., Bishop, M.P., Shroder, J.F., 2001. Erosion, Himalayan geodynamics, and the geomorphology of metamorphism. GSA Today 11, 4–9.

Zeitler, P.K., Meltzer, A.S., Brown, L., Kidd, W.S.F., Lim, C., Enkelmann, E., 2014. Tectonics and topographic evolution of Namche Barwa and the easternmost Lhasa block, Tibet. Spec. Pap., Geol. Soc. Am. 507, 23–58. https://doi.org/10.1130/2014.2507(02).

Zhang, J.Y., Yin, A., Liu, W.C., Wu, F.Y., Lin, D., Grove, M., 2012. Coupled U–Pb dating and Hf isotopic analysis of detrital zircon of modern river sand from the Yalu River (Yarlung Tsangpo) drainage system in southern Tibet: constraints on the transport processes and evolution of Himalayan rivers. Geol. Soc. Am. Bull. 124, 1449–1473. https://doi.org/10.1130/B30592.1.